Aluminum U–Groove Weld Enhancement Based on Experimental Stress Analyses

V. Verderaime and R. Vaughan

Aluminum U–Groove Weld Enhancement Based on Experimental Stress Analyses

V. Verderaime and R. Vaughan
Marshall Space Flight Center • MSFC, Alabama

ACKNOWLEDGMENTS

TABLE OF CONTENTS

LIST OF ILLUSTRATIONS

LIST OF TABLES

NOMENCLATURE

a = weld width, inch

c = coefficient

C = y - boundary, inch

E = elastic modulus, ksi

F = material strength, ksi

H = specimen thickness, inch

h = weld pass thickness, inch

K = inelastic strength coefficient

l = weld to pin distance

M = induced moment, inch-kips

N = applied axial load, kips

n = strain hardening exponent

      = total number of weld passes

m = weld sequence number

T = temperature, °F

t = U-groove tabs, inches

w = specimen width, inch

α = coefficient of thermal expansion, in/in/°F

δ = peaking eccentricity, inch

ε = strain, in/in

σ = stress, ksi

v = Poisson's ratio

ϕ = peaking angle

Subscripts

A = maximum surface strain

B = minimum surface strain

e = elastic

i = strain gauge number

     = weld pass series

j = weld pass number

$,k$ = designated temper

M = moment

N = axial load

o = elastic limit

     $= x = 0$

p = inelastic

q = limit of interest

tu = tensile ultimate

ty = tensile yield

x,y,z = coordinate axes

α = thermal relate

TECHNICAL PAPER

ALUMINUM U-GROOVE WELD ENHANCEMENT BASED ON EXPERIMENTAL STRESS ANALYSES

I. INTRODUCTION

Joints are the lowest specific strength links in the chain of high-performance structures. Their initial manufacturing cost and their recurring inefficient performance costs are compelling incentives to penetrate their unique mechanics for designing more affordable structures delivered to space. Butt-welds are among the most preferred joining methods in aerostructures because their permanent sealing integrity and their elastic behaviors are indistinguishable from base structures, but their inelastic performances are generally the least understood. As structural environments and component sizes increase, butt-weld thicknesses increase, weld development and processes become more complex, and joint strengths are less predictable. This study investigated the experimental strain distribution across an aluminum double U-grooved weld and identified process design variables and sensitivities that should improve strength performance.

Thick butt-welds are most likely to be employed on large aluminum plates and shell structures. Their unique multipass process characteristics, their costly developments, and their inelastic properties encompassing traditional ultimate safety factors are strong incentives for understanding and improving weld design techniques. However, the many inelastic variables that must be characterized from a single first-loading to fracture test per specimen make scientific experimental research (one controlled parameter explored at a time) very costly. Consequently, stress investigators are too often challenged to model performance and verify it from the broader and less decisive laboratory-type experimental data.

One early study modeled a uniaxial butt-weld specimen having different lateral contraction rates between preweld material and homogeneous weld filler and discovered a metallurgical discontinuity at the interfaces[1] upon exceeding the elastic limit. The physical model revealed a transverse shear spike just below the surface, at the filler interface, which had been first observed by Paul Munafo in fractured surfaces of thick aluminum uniaxial test specimens. This was an interesting discovery in explaining why the interface was the weakest region in the weld structure. The study further questioned the metallurgical discontinuity effects of weld strength design data derived from prevailing uniaxial tests with that of the biaxial strengths expected in girth and longitudinal welds used on pressure vessels.

Discontinuity stresses noted in the above study, especially transverse shear, were later experimentally verified[2] on a thick-weld cross section in uniaxial test. Transverse shear could not be directly measured experimentally but was calculated from closely spaced strain gauge data. Because the width of the shear spike was about the same as the strain gauge spacing, only an averaged shear stress was verified rather than the full tip intensity of the narrow sharp spike. This test measuring deficiency is similar to that noted in finite element methods (FEM) using coarse grids. Neither the analytical nor experimental investigations considered the welding thermal effects and residual strains on filler material properties.

A recent experiment conducted on 2219-T87 aluminum butt-welds developed and documented[3] extensive photostress and electric strain gauge test data. The strain gauge data along the weld center line and along the heat-affected-zone (HAZ) revealed varying strain distributions across the specimen thickness under uniaxial loading. A formal strain analysis was not scoped in that task. Another study[4] used the experimental weld data to model the plastic material properties of the weld across the thickness. It assumed a simplified uniform axial stress and correctly concluded that the weld filler stiffness varied among the weld passes.

While a previous paper established and modeled the discontinuity stresses at the preweld metal and weld filler interface, this study endeavored to explored the multipass welding process and resulting structural behavior of weld filler passes. Each intrinsic material and structural variable investigated invoked a unique assumption and technique for elastic-inelastic modeling of weld behavior from experimental data. Because of the nature of the laboratory-type experiment, designer control parameters were identified and characterized only to a first-order-analysis with the hope of providing a higher-order-understanding and techniques for improving thick weld joint designs at least cost.

II. WELD SPECIMEN

The multipass aluminum butt-weld specimen tested was of the same configuration, materials, and process developed for a critical aerostructural component. The specimen was instrumented and uniaxially tested. Experimental data sources are referenced, and data specifically used in this investigation are repeated.

A. Configuration

The aluminum test specimen is a double U-grooved butt-weldment that was machined from 2219 milled plate welded to a forged panel. The weld filler is 2319 aluminum with the beads ground off, as shown in figure 1.
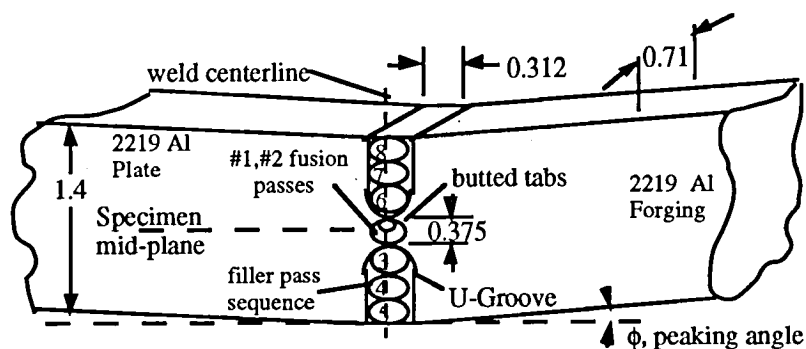
Figure 1. Test specimen configuration.

The specimen thickness is $H = 1.4$ in and the width is $w = 0.71$ in, giving a cross section area of approximately 1 in^2. The butted tab thickness between the grooves is $t = 0.375$ and the distance between end pin connections is 12.5 in. The peaking angle ϕ is an unintentional angular displacement resulting from a normal weld schedule process and was estimated to be less than 0.02 radians.

Welding process structural variables causing the peaking angle required identification and their sensitivities assessed.

B. Structural Process

The specimen was TIG welded. The butted tabs between the double U-grooves were tack fusion welded followed by continuous fusion welding from the same side. Subsequent welds were filler passes serially applied, first in the groove opposite pass No. 1, and then on the reverse side groove noted in figure 1, for a total of eight passes. Filler pass contact temperature was approximately 640 °F, which produced local thermal expansion followed by weld contraction and tensile straining upon cooling. Weld temperature conducted just below the weld pass was sufficient to anneal the lower weld pass and then to contract and strain it in tension upon cooling. The completely welded specimen was observed to have peaked with the obtuse angle on the last weld pass side. The specimen was heat treated to 350 °F for 18 h. Thermal straining variables and effects on weld peaking and depeaking were modeled from the following thermal-stress process.

Weld pass No. 1 in figure 1 was crucial to the butted edge mismatch.[5] In this weld pass, the double U-groove tabs at the midplane were butted, the panel surface planes were aligned, the assembly was constrained, and the butted tabs were fusion tack welded (without filler material) on one side. The tack weld pass produced local thermal expansion on the butted tabs and was followed by cooling contraction. The cooling induced a tensile strain on the tack weld side and compression on the unfused side of the tab. This tension on the one side of the butted tabs and contact compression on the other side peaked the panels with the obtuse angle on the tack welded (tension) side. Peaking from combinations and tolerances of these initial process variables varies from one structure and design to another and fades with the second pass.

The intense weld heat input of pass No. 2 produced the objectionable peaking angle. It was another fusion weld pass applied on the same side of the tack weld, but having the highest heat input rate to fuse the total tab thickness, which is about a quarter of the specimen thickness. The associated extreme thermal expansion and contraction gradient across the tab thickness produced the maximum peaking angle in the process with the obtuse angle again on the heat source side (tack weld side).

The next three passes were weld filler passes requiring less heat and were applied in the groove opposite the No. 1 tack pass side. Each weld pass produced a thermal gradient and expansion across the welded section and, at the same time, annealed the weld structure below it. Upon cooling, the confined filler pass contracted inelastically and then elastically in tension, which bent and strain hardened the tabs and built-up filler passes and reduced the peaking angle produced by the second fusion weld pass. Subsequent weld passes were applied on the opposite groove, producing less thermal straining but moderately increasing the panel peaking.

The extent of peaking at any point in the process depends basically on the initial peaking from the fusion passes and the peaking and depeaking contributions of successive filler weld passes at that point into the process. Increasing the laid-up weld thickness increases the section modulus, which stiffens and reduces the panel deflection rate induced by the succeeding thermally contracted filler pass. It then follows that successive thermal bending and strain hardening become negligible, and that the net peaking angle is governed by the specimen side accumulating the most and earliest thermal tensile straining. This was the basis for developing a math model to qualitatively select the process option that minimizes the weld peaking.

The peaking angle ϕ_m, for any pass $j > 2$ and at sequence m in the welding process, may be expressed by

$$\phi_m = \phi_2 + \sum_{j=3}^{m} s_j \phi_j \ , \tag{1}$$

where the first term is the initial peaking angle ($\phi_2 > \phi_3$) produced by the fusion welds on the U-groove tabs and the second term is the sum of subsequent depeaking and peaking weld passes for $j \geq 3$. The coefficient "s" polarizes the weld pass sequence where $s = +1$ refers to the peaking weld pass applied in the groove on the weld pass No. 1 side of the midplane, and $s = -1$ refers to the depeaking pass applied in the opposite groove. Developing an absolute model of equation (1) for a variety of materials, geometries, and processes could be formidable if not remote. It will be shown that reversing the peaking side is more beneficial than totally eliminating it.

Figure 2 qualitatively modeled the weld peaking behavior of the jth pass in the welding process for identifying associated structural variables, trends, and sensitivities which might reduce peaking. The peaking angle ϕ at the jth weld pass was derived with designer control variables, which are the weld pass thicknesses, h_i, the polarity, and the accumulated thickness. Passive control variables, such as material constants and unique coefficients, were lumped into unquantified coefficients leading to versatile qualitative expressions.
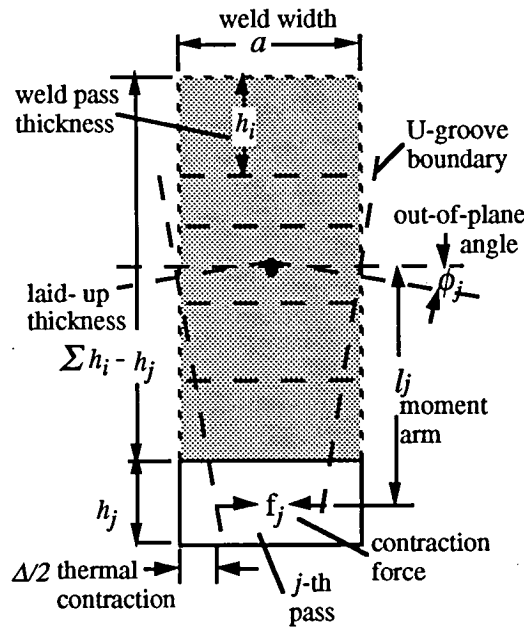
Figure 2. Peaking angle from jth weld filler pass.

Assuming a unit weld length, the confined cooling contraction of the jth weld pass induces a tensile force of

$$f_j = \sigma_\alpha h_j \ , \tag{2a}$$

where the thermal stress is derived from the filler thermal contraction equated to the stress tension displacement,

$$\Delta = a \alpha T = a \frac{\sigma_\alpha}{E} \ , \tag{2b}$$

4

and is reduced to

$$\sigma_\alpha = \alpha E T. \qquad (2c)$$

Substituting equation (2c) into (2a) and using the moment arm defined in figure 2, the moment imposed by the thermal contraction force about the centroid of the accumulated weld passes is

$$M_j = f_j s_j \left[\frac{1}{2} \sum_{2}^{j} h_i \right] = \frac{1}{2} \alpha E T s_j h_j \sum_{2}^{j} h_i \ , \qquad (3a)$$

and the resulting peaking angle of the stub filler was approximated by a third degree stress function[6]

$$\phi_j = \frac{c_1 M_j a}{E \left(\sum_{2}^{j} h_i - h_j \right)^3} \ . \qquad (3b)$$

Substituting equation (3a) into equation (3b) and separating the unique fusion pass angle, the peaking angle induced by the jth weld pass is expressed by

$$\phi_j = \frac{c s_j h_j \sum_{2}^{j} h_i}{\left(\sum_{2}^{j-1} h_i \right)^3} \ . \qquad (4)$$

Sensitivity of the peaking angle to the designer controlled weld pass thickness is

$$\frac{\partial \phi_j}{\phi_j} = \frac{\partial h_j}{h_j} \ , \qquad (5a)$$

where increasing the weld pass thickness increases the cooling contraction force defined by equation (2a). Peaking angle sensitivity to a large number of accumulated weld passes is

$$\frac{\partial \phi_j}{\phi_j} = -2 \frac{\partial \sum_{2}^{j-1} h_i}{\sum_{2}^{j-1} h_i} \ , \qquad (5b)$$

where the peaking angle decreases as the buildup thickness increases, which increases the bending moment resistance expressed by equation (3b). Though the peaking angle is seen to be more sensitive to accumulated passes, it is not mutually exclusive of the weld pass thickness, and the optimum schedule must consider both in a least-cost manufacturing process.

Substituting equation (4) into the second term of equation (1) and solving for the depeaking angle at the end of the mth sequence,

$$\phi'_m = \phi_m - \phi_2 = \sum_{j=3}^{m} s_j \phi_j \ ,$$

or

$$\phi'_m = c_\alpha Z_m \ , \tag{6}$$

where the desired depeaking index is expressed by

$$Z_m = Z_2 + \sum_{3}^{m} \frac{c\, s_j h_j \sum_{2}^{j} h_i}{\left(\sum_{2}^{j-1} h_i\right)^3} \ . \tag{7}$$

The depeaking index of equation (7) was applied to the normal welding schedule of figure 1, having a uniform filler weld pass thicknesses of

$$h_i = \frac{(H-t)}{n-2} \ , \tag{8a}$$

$$h = \frac{(1.4 - 0.375)}{8 - 2} = 0.171 \ .$$

Substituting the uniform filler thickness into equation (7), the depeaking index after the $m = 5$ pass is

$$Z_5 = -\frac{0.17(0.375 + 0.17)}{(0.375)^3} - \frac{0.17(0.375 + 2(0.17))}{(0.375 + 0.17)^3} - \frac{0.17(0.375 + 3(0.17))}{(0.375 + 2(0.17))^3} = -3.34 \ ,$$

and after $m = n = 8$ is

$$Z_8 = Z_5 + \frac{0.17(0.375 + 4(0.17))}{(0.375 + 3(0.17))^3} + \frac{0.17(0.375 + 5(0.17))}{(0.375 + 4(0.17))^3} + \frac{0.17(0.375 + 6(0.17))}{(0.375 + 5(0.17))^3} = -2.78 \ .$$

Depeaking indices after each filler pass are listed in figure 3 for a normal weld schedule. Since the specimen showed a peaking angle of 0.02 radians, the peaking index was $Z_2 > +2.8$, and the normal weld schedule proved to be insufficient.
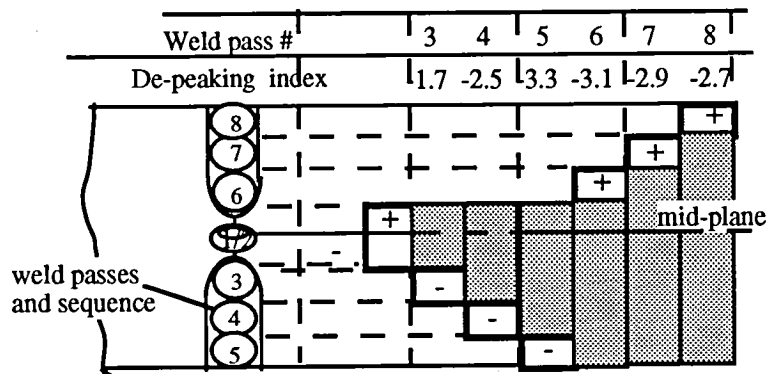
Figure 3. Depeaking index for normal weld schedule.

Figure 4 illustrates an unconventional weld pass schedule assuming the same filler pass thickness as in figure 3, but the U-groove tabs were off-centered by one pass to provide an additional depeaking weld pass. The off-centered tabs schedule should reverse the peaking angle for a net weld strength increase to be shown later.

Weld pass #	3	4	5	6	7	8
De-peaking index	1.7	-2.5	3.3	-3.6	3.4	-3.3

weld passes and sequence

mid-plane
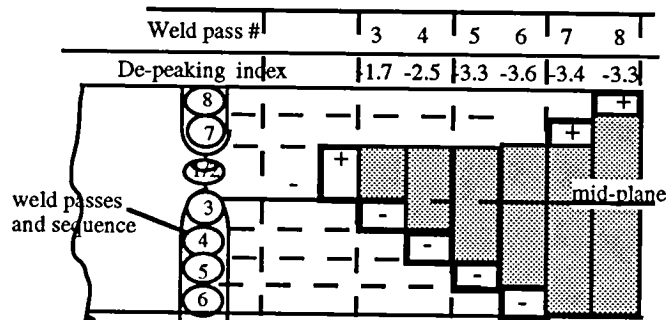
Figure 4. Accumulated peaking angles for unsymmetrical weld schedule.

Other weld schedule options with centered tabs were assessed through equation (7). Increasing the welds to four thinner filler passes on the peaking side for a total of nine filler passes provided an index of −2.82, and it was not better than the normal weld schedule. Increasing the weld passes to 10 uniform filler thicknesses provided a worse index of −1.9.

C. Instrumentation

The specimen was instrumented to obtain strain data during a sequence of uniaxially applied loads on the test specimen as reported in reference 3. A total of 10 electrical strain gauges was oriented to obtain axial strain measurements along the specimen thickness. Strain gauges 1 through 5 were installed equidistant across the specimen thickness along the weld centerline. Another five gauges, 6 through 10, were installed on the forging $1/2$ in away from and parallel to the weld center line, as shown in figure 5, to provide the strain distribution along the HAZ. Electrical strain gauge sizes were $1/32$ in, having an accuracy of ±10 micro inches at constant temperature, and were bonded with M-Bond™ 200 adhesive.

top face gage numbers

filler pass sequence

U-Groove tabs

1,2 fusion passes

strain gages

0.34" (typ.)

specimen mid-plane

X

weld centerline

0.5"

HAZ

bottom face gages
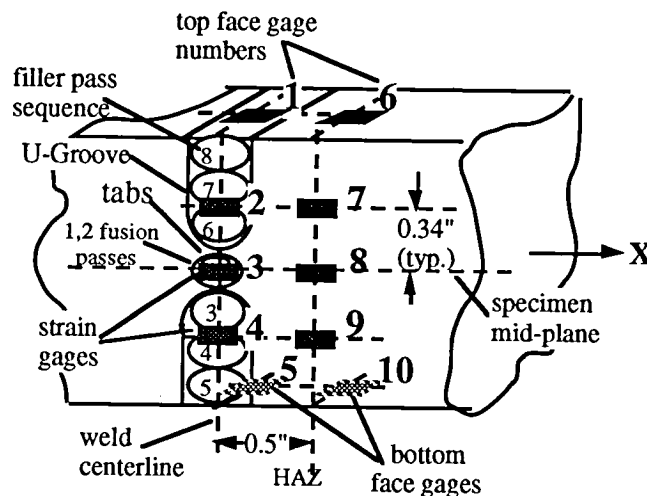
Figure 5. Strain gauge locations and orientation.

Photoelastic coating was bonded with PC-8™ adhesive to provide regional qualitative and quantitative strain distribution pattern across the weld thickness under uniaxial loading. Photos of fringe patterns at representative loading intensities were documented in reference 3. The specimen was loaded on a SATEC 55 uniaxial testing machine to levels below weld fracture.

IV. DATA ANALYSES

To improve the thick-weld filler strength, it was necessary to explore its uniaxial structural behavior beyond the elastic limit and its imposed environments and sources. The environments were first identified on the homogeneous HAZ and verified through response models using experimental strain data in table A1, and bending and normal loads were determined from structural models in appendix C. The inelastic, nonhomogeneous properties of weld filler passes were derived from moment equilibrium considerations. As in most testing appliances, mechanical friction and play make the accuracy of the smallest experimental measurements suspect and should avoid differences between small measurements with single significant digits.

A. HAZ Strain Analyses

Because of the HAZ homogeneity, its common elastic-inelastic material properties were easiest to characterize from strain data, from which external environmental sources and influences on strain response might be more readily identified and defined. Figure 6 is the HAZ strain gauge data response across the specimen thickness plotted against increasing applied axial loading, as listed in table A1.
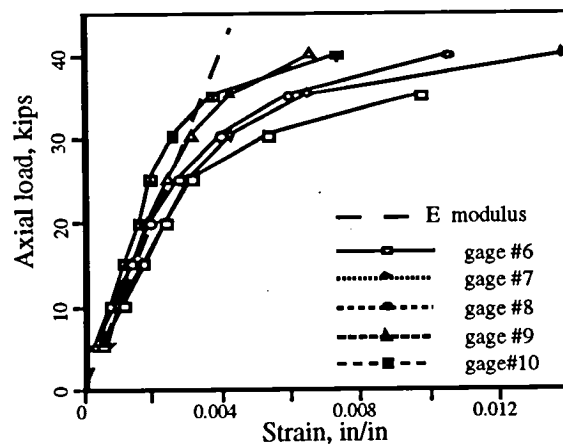
Figure 6. HAZ strain distribution versus axial loads.

If the HAZ material were homogeneous and the axial load were applied uniformly across the thickness, the five load-strain data points across the specimen thickness should have coexisted at each loading increment to form a single curve defined by equation (B1). Furthermore, the elastic response should have coincided with the elastic modulus imposed on figure 6. However, the fan-out and sequential order of the elastic and strain hardening slopes were indications that the specimen was subjected to combined axial and bending loads. It also suggested a more appropriate cross-plot of the same HAZ strain data but as a function of gauge location across the specimen thickness, as illustrated in figure 7.

8
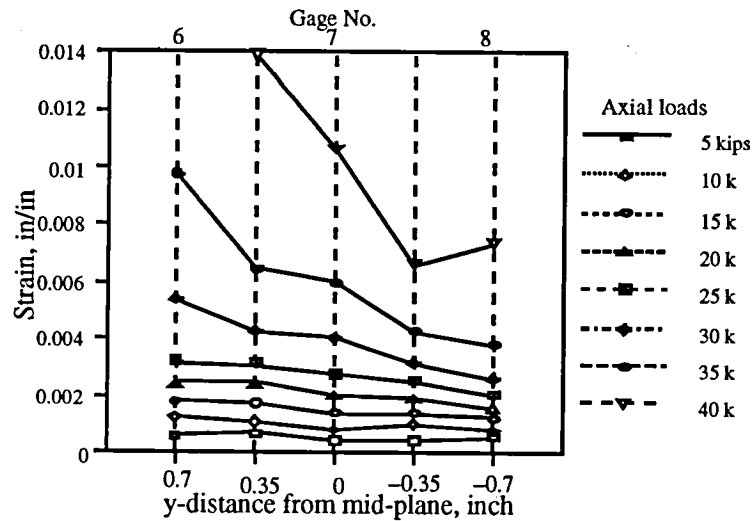
Figure 7. Strain distributions across the HAZ thickness.

The curves' uniformly increasing slopes with increasing axial loads confirmed the existence of an increasing induced bending moment. Their straight line trend seemed to comply with planes in homogeneous structures remaining plane after elastic and inelastic bending. The strain slopes across the specimen thickness first increased uniformly and steadily and then rapidly with uniformly increasing axial load. This behavior conformed to the elastic and inelastic increased strain response rates, respectively, defined by the strain hardening exponent in equation (B1).

Line offset strains, measured by gauges No. 7 and No. 9, occurring during inelastic loading (N > 20 kips), are most likely due to the inelastic boundary strain transmitted by nonhomogeneous weld filler stiffness behavior in the adjacent U-grooves. This strain pattern is seen to be amplified in figure 8, which establishes the source. The fact that surface mounted strain gauge No. 6, in figures 6 and 7, experiences greater tension response than others clearly demonstrates that bending tension occurs on the side of the last weld pass in a normal weld schedule. The excessive strain indicated by gauge No. 10 at 40 kips cannot be explained, especially when the adjacent gauge No. 5 in figure 10 behaved as expected.
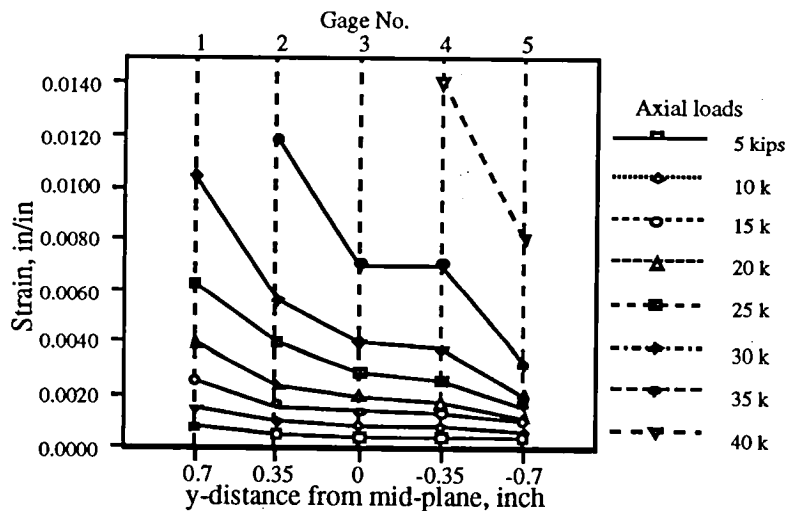
Figure 8. Strain distribution across weld filler thickness.

The yield point is the interface between the elastic and inelastic structural properties modeled by equation (B1),

$$\sigma_{ty} = E\,\varepsilon_{ty} = K\,\varepsilon_{ty}^{n} \; , \tag{9}$$

and is crucial to identifying and defining material properties from the experimental strain data. Strains at surface mounted gauge No. 6 in figure 6 were seen to depart from a constant strain rate under constant loading rate at about 25-kips load. The strain slope at 25-kips axial load in figure 7 provided a more distinctive indication of the elastic-inelastic transition, with strain gauge No. 6 assuming the maximum elastic strain of $\varepsilon_{ty} \approx 0.003$ (table A1).

Applying this yield strain in equation (9) to calculate the yield stress and substituting the stress into equations (B4) and (B5), the HAZ material elastic-inelastic properties were approximated as

$$E = 10{,}500 \text{ ksi}, \; F_{ty} = 33 \text{ ksi}, \; F_q = 58 \text{ ksi}, \; \varepsilon_{ty} = 0.0031, \; \varepsilon_q = 0.06, \; n = 0.191, \; K = 99.3 \text{ ksi} \; .$$

Though the specimen was heat treated for T87 condition after welding, the calculated yield stress of the HAZ forging is more like a T6 condition (table B1) for lack of sufficient work hardening.

Substituting these calculated HAZ properties and the specimen cross section of $H = 1.4$ and $w = 0.71$ inches into the appendix C program, the axial load, the induced bending moment, and eccentricities were determined for each increment of loading using related pairs of surface measured strains (gauges No. 6 and No. 10) listed in table A1. The totally induced bending moment M reflected by strain data consisted of the axial load N acting on the specimen geometric eccentricity combined with the material stiffness eccentricity. The total eccentricity is given by

$$\frac{M}{N} = c_s \delta + C_M \; . \tag{10}$$

The peaking eccentricity δ resulted from the welding process discussed before, and c_s is the straightening coefficient which varies with increasing axial load. This geometric eccentricity induced a maximum bending tensile strain on one side of the specimen which, combined with the applied uniform tensile axial strain, produced a maximum tensile strain at one surface. Subsequent loading initiated inelastic strains on that surface that progressed through the cross section producing inelastic and elastic zones across the specimen thickness. The related inelastic and elastic moduli (stiffness) zones across the thickness shifted the bending neutral axis C_M away from the midplane to maintain moment equilibrium acting on the plane. This shift is illustrated by figures C1 and C2. Thus, the bending neutral axis shift, C_M, in equation (10) is noted as the material eccentricity, which was triggered at the onset of the specimen material exceeding the elastic limit ($C_M > 0$), and it bears the same polarity as the geometric eccentricity that precipitated it.

Table 1 lists experimental strain data, used to determine axial loads and moments from the appendix C program, and the resulting eccentricities calculated from equation (10). The tabulated variation of the geometric eccentricity $\delta\,c_s$ throughout the elastic loading ($C_M < 0$) required examination.

Table 1. Specimen induced loads and eccentricities in HAZ.

Variables	5 kips	10 kips	15 kips	20 kips	25 kips	30 kips
Gauge No. 6	0.0006	0.0012	0.0018	0.0024	0.0032	0.0054
Gauge No. 10	0.0005	0.0008	0.0012	0.0015	0.0020	0.0026
N kips	5.740	10.43	15.65	20.87	27.28	33.80
M kips-in	0.121	0.487	0.730	0.974	1.488	6.129
C_M in	0	0	0	0	–0.001	–0.162
M/N in	0.021	0.047	0.047	0.047	0.055	0.186
δ_{CS} in	0.021	0.047	0.047	0.047	0.054	NA

B. Induced Elastic Bending

Though the peaking eccentricity may be measured on the specimen, or the geometric eccentricity calculated from experimental strain data, as in appendix C, its elastic behavior and the designer control parameters' influence on the induced bending moments had to be identified and the source verified. Figure 9 is a sketch of one welded panel of the symmetrical specimen (fig. 1) illustrating the peaking angle geometries and loading variables.
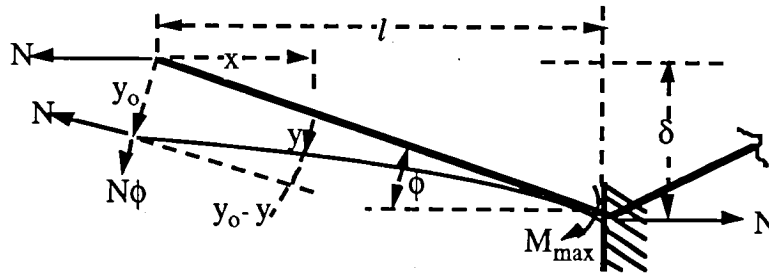
Figure 9. Induced bending moment model.

The peaking angle

$$\phi = \frac{\delta}{\ell} \ ,$$

(11)

is usually very small, such that the projected axially applied load in the plane of the panel was assumed to be $N \cos \phi = N$ and the projected normal to the panel was assumed to be $N \sin \phi = N\phi$. These assumptions reduced the model to a beam with a transverse load $N\phi$ and tensile axial load N. The axial tension load tends to straighten the beam and reduce the bending moment rate produced by the transverse load $N\phi$. The differential equation of the deflection curve caused by the transverse bending and the axial straightening moments and was represented by

$$\frac{d^2y}{dx^2} = -\frac{M}{EI} = (N\phi x - N(y_o - y))\frac{1}{EI} \ ,$$

(12)

which is of the form

$$\left(D^2 - \frac{N}{EI}\right) = \frac{N}{EI}(\phi x - y_o) \ .$$

11

Using the notations

$$k^2 = \frac{N}{EI} \quad \text{and} \quad EI = \frac{EwH^3}{12} \ , \tag{13}$$

and minding the tensile axial load is negative, the general solution of equation (12) is

$$y = A_1 \sinh kx + A_2 \cosh kx + \phi x - y_o \ . \tag{14}$$

Applying boundary conditions $y = y_o$ at $x = 0$ and $y = 0$ at $x = 1$ to the deflection equation (14), and differentiating and letting the slope vanish at $x = 1$, the constants of integration were determined,

$$A_1 = -\frac{\phi}{k \cosh kl} \quad \text{and} \quad A_2 = 0 \ ,$$

and the end deflection is

$$y_o = \phi l - \frac{\phi}{k} \tanh kl \ . \tag{15}$$

Substituting the integration constants and end deflection into equation (14) provided the welded panel deflection expression,

$$y(x) = -\frac{\phi}{k} \frac{\sinh kx}{\cosh kl} + \frac{\phi}{k} \tanh kl + \phi \ (x-l) \ . \tag{16}$$

Differentiating equation (16) twice, the moment equation is defined as

$$M(x) = EI \frac{d^2y}{dx^2} = -\phi k \ EI \frac{\sinh kx}{\cosh kl} \ . \tag{17}$$

The maximum moment at the weld $(x = l)$ is given by

$$M_{\max} = -EI \ k \frac{\delta}{l} \tanh kl \ ,$$

and substituting the first notation of equations (13), the induced elastic bending moment at the weld was modeled by

$$M_{\max} = -N \frac{\delta}{l} \sqrt{\frac{EI}{N}} \tanh \left(l \sqrt{\frac{N}{EI}} \right) \ . \tag{18}$$

For a given peaking eccentricity δ, the ratio M/N in equation (18) was seen to decrease with increasing axially applied tensile load through the elastic straightening coefficient

$$c_s = \frac{M_{\max}}{N \delta} = l \sqrt{\frac{N}{EI}} \coth \left(l \sqrt{\frac{N}{EI}} \right) \ . \tag{19}$$

Applying the HAZ elastic properties estimated above and using a length $l = 6.0$ inches in equations (18) and (19), the moments and geometric eccentricities listed in table 1 were assessed for $C_M = 0$. The geometric eccentricity $c = 0.021$ at 5-ksi loading seemed too small, and it was due to the familiar error of differences of round-off single digits. An eccentricity of 0.047 might have been

12

produced, if the two surface strains included a second digit as 0.00045 and 0.00065. The $\delta c_S = 0.047$ eccentricities in table 1 were noted to be constant through the elastic loading range, which was contrary to equation (19). An explanation might be that a resisting moment was imposed at the specimen end-connections by the static friction acting on one-inch diameter pins. The sudden increase to $\delta c_S = 0.055$ may have resulted from the 25-kips applied load overcoming the static friction moment.

The sensitivity of the maximum bending moment at the weld to the peaking eccentricity was derived from equation (18) and was expressed by

$$\frac{\partial M_g}{M_g} = \frac{\partial \delta}{\delta} , \qquad (20)$$

as a direct proportionality. The moment sensitivity to the term lk was derived as

$$\frac{\partial M_g}{M_g} = \frac{1}{\cosh lk \sinh lk} \frac{\partial lk}{lk} . \qquad (21)$$

The moment sensitivity decreased as the term lk increased, which decreased the straightening effect. The bending moment sensitivity to the peaking eccentricity of equation (20) is a welding process control variable. The moment sensitivity to lk of equation (21) is primarily influenced by the thickness H and is a stress designer control variable. Increasing the thickness will increase the bending stress caused by the geometric eccentricity, but it must be optimized with the dominant stress produced by the axial load.

C. Weld-Filler Properties

The complex thermal and stress strains, work-hardening, and annealing environments uniquely experienced by each weld pass were discussed in the welding process above. The question still persisted as to how unique the structural properties of each weld pass after the final heat treatment are and which of the passes has the lowest ultimate stress. Because the microstructure of the specimen materials is basically face centered cubic lattice, the 2219 HAZ and the 2319 weld filler structures were expected to behave homogeneously with a common elastic modulus up to the onset of inelastic strain anywhere among the weld passes. The distinguishing onset of inelastic properties of each weld pass was the yield point, from which the strength coefficient and strain hardening exponent were estimated from equations (B4) And (B5). The analysis was carried only to an order of approximation necessary to verify variations of properties and sources of variations along the cross section that might be controlled to improve weld design or to enhance its applications.

Figure 8 illustrates table A1 measured strain distributions along the weld filler cross section similar to the HAZ distributions in figure 7. As in the HAZ, the elastic strain response of the filler to increments of axial loading was seen to produce planes of uniformly varying strains along the cross section, which was indicative of bending of a homogeneous material. However, higher inelastic strain responses were experienced by the filler than by the HAZ, and strains no longer remained in planes for common increments of axial loading, all of which clearly signified softer, nonhomogeneous zones of filler materials.

There were only five strain gauges to resolve properties of eight weld passes. Figure 5 displayed surface mounted gauges No. 1 and No. 5 measured strains from weld passes No. 8 and No. 5,

respectively. Gauge numbers 2, 3, and 4 measured average strains from pairs of weld pass numbers 7 and 6, 1 and 2, and 3 and 4, respectively. The transition from elastic to inelastic strain in each weld pass was spotted in table A1 data by the on-set change of constant strain rate to a suddenly increased rate under constant loading rate. And because of the induced bending moment, the on-set of yield strain was noted to occur at one gauge at a time and sequentially, with successively increasing increments of axial loading.

The transition from elastic to inelastic strains was seen to occur at levels in excess of 0.002 in/in on gauges 1 through 5 and under uniaxial loading of 15 through 35 kips. The yield stresses were calculated from the noted yield strain, and the weld pass properties represented by respective gauges and applied axial loads were approximated through the load equilibrium equation

$$N = wh \sum_{i=1}^{5} K_i \varepsilon_i^{n_i} p_i \ ,$$

or

$$\frac{N}{wh} = \sum K \varepsilon_p^n p + E \sum \varepsilon_e p \ , \tag{22}$$

where the first and second terms on the right of equation (22) are the sum of inelastic ε_p and elastic ε_e measured strains, respectively. The weld pass thickness was assumed to be equally divided along the thickness for an average of $h = H/8 = 0.175$ in, and "p" is the number of passes represented by each respective strain gauge. This technique was applied to all five gauges to identify and define weld pass inelastic properties along the weld centerline.

In applying table A1 strain data for the applied load $N = 10$ kips into equation (22), all strains were noted to be elastic ($\varepsilon < 0.002$) and the elastic modulus was calculated to be about 2 percent greater than the commonly used milled plate value of $E = 10,500$ ksi. This was as much a check on elastic strain data quality as it was a verification on the filler elastic modulus.

Proceeding with filler properties determinations from strains induced at the next increment of loading $N = 15$ kips, at least one strain had to be inelastic to not exceed the load equilibrium of equation (22). That inelastic strain had to be greater than 0.002 and on the verge of a strain rate increase. This strain was measured by gauge No. 1 at $\varepsilon_1 = 0.0026$. Substituting the inelastic and all elastic strains induced at $N = 15$ kips into equation (22),

$$pK(0.0026)^n = \frac{15}{0.124} - 10,500(0.001 + 2(0.0016 + 0.0014 + 0.0013)) \ ,$$

where $p = 1$, the inelastic stress was,

$$K(0.0026)^n = 20.2 \text{ ksi} \ . \tag{23a}$$

By trial (or Newton method), a yield stress was selected and applied into equations (B4) and (B5) to satisfy equation (23a) and the resulting properties representing weld pass No. 8 were listed in table 2. Given that pass No. 8 filler did not fracture under the maximum axially applied test load of 45 kips, a condition on the derived inelastic properties was that the ultimate stress must exceed 45 ksi. Assuming an ultimate yield of $F_{ty} \geq 0.06$ in equation (B1), that condition was satisfied.

At 20-kips loading, the inelastic weld pass properties to be determined were No. 6 and No. 7 represented by gauge No. 2. Substituting the above derived inelastic properties of weld pass No. 8 in

14

equation (B1) and continuing as with the 15-kips loading case, the load equilibrium of equation (22) was

$$2K(0.0024)^n = \frac{20}{0.124} - 94.7(0.004)^{0.254} - 10{,}500(0.0012 + 2(0.002 + 0.0018)) \ ,$$

and the stress was

$$K(0.0024)^n = 22.8 \text{ ksi} \ . \tag{23b}$$

Results from similarly derived inelastic properties at all five strain gauges along the weld center line are listed in table 2.

Table 2. Weld filler inelastic properties.

Gauge Numbers	1	2	3	4	5
Weld Pass Numbers	8	7, 6	1, 2	3, 4	5
Properties					
F_{ty} ksi	19	22	27	37	30
n	0.245	0.241	0.218	0.174	0.205
K ksi	94.7	97.3	99.3	98.6	99.7
σ_q ksi	46	49	53	58	56
ε_{ty} in/in	0.0018	0.0021	0.0025	0.0035	0.0028
ε_q in/in	0.06	0.06	0.06	0.06	0.06

In the above load equilibrium analysis, inelastic properties of one weld pass to another were primarily distinguished by their yield stress. The 2219 butted U-groove tabs at the weld center line are plate material and were expected to exhibit a higher yield stress than the casting-like 2319 weld filler material. Gauge numbers 2, 3, and 4 in figure 8 implied it by the counterclockwise strain pattern. And though results from equation (22), listed in table 2, confirmed the suspected variation of inelastic properties among the weld passes, the orderly decrease of filler yield stress correlated with the orderly increase in weld pass sequence. The last weld pass No. 8 at gauge No. 1 was noted to have the lowest yield property, the prior pass had the next lowest yield property, and etc. This phenomenon was verified by an independent graphic analysis, which plotted logs of table A1 data and intercepted them with the log of the elastic modulus, and obtained similar yield straining order and magnitudes.

This decreasing filler pass yield stress with increasing sequence pass is a particularly interesting phenomena in that it coincides with the decreasing peaking index expressed by equations (5b) and (7). Since weld depeaking and strain hardening decreases with increasing passes, later filler passes experience less strain hardening, which acquire less heat treatment and lower yield stress. Consequently, if the weaker last pass filler (on obtuse angle of the specimen) is combined with the tension component of the induced moment, the last pass filler will prematurely rupture under uniaxial loading. A significant improvement would be to depeak the weld sufficiently to reverse the obtuse angle on the first pass side in order to induce the tension component of the moment on the earlier passes having higher yield stresses and strength.

Because inelastic strains span three orders of magnitude over a stress increase factor of less than 2, and because stress is a more common and convenient judgment parameter of structural behavior, the strain data in table A1 was converted into stress and listed in table 3 using equation (B1).

Table 3. Axial load versus weld filler stresses based on table A1.

Gauge Numbers	1	2	3	4	5
Weld Pass Numbers	8	7, 6	1, 2	3, 4	5
Axial Loads, N					
5 kips	8.4	5.2	4.2	4.2	4.2
10	16	11	9.5	8.4	6.3
15	21	17	15	14	11
20	23	23	21	19	13
25	26	25	28	27	17
30	30	28	30	37	21
35	35	33	34	42	31

The tabulated stresses were further plotted in figure 10.
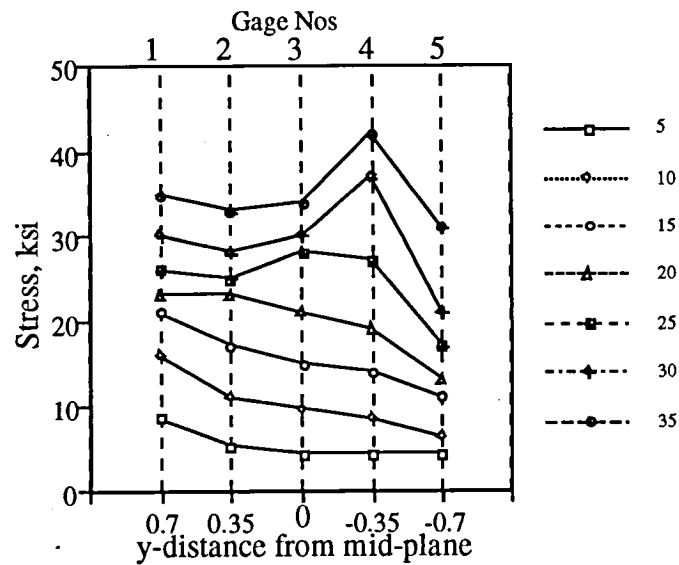
Figure 10. Stress distribution across weld filler section.

The stress distributions in figure 10 clearly illustrated the initial uniform variation of an homogeneous material under axial and bending loads, and then the abrupt increase at the midplane at $N =$ 25-kips loading as though dominated by a stiffer material, such as the butted tabs and earlier filler pass. Higher yield stress material along the specimen cross section sustained a larger share of the applied axial load and resisted more of the induced moment.

Though the inelastic analyses and resulting stress distribution in figure 10 were derived for "first loading" only (subsequent loading distributions are elastic up to the highest previous loading),

16

fracture is still predicted at the weld pass having the yield stress established by the "first loading" and at the ultimate stress estimated by equations (B4), (B5), and (B1). The weakest filler pass is listed in table 2 as weld pass No. 8, and it is the last weld pass. Had the welding process selected the weld schedule in figure 4, the excess depeaking might have produced an obtuse angle on the opposite surface (pass No. 6) having a higher yield and ultimate strengths and thus improved the net U-groove weld strength.[8]

D. Photostress Correlation

Photostress techniques were applied to the weld specimen to complement the strain gauge data analyses. Representative results for the combined axially applied load and bending moment induced by peaking eccentricity depict the highest straining to initiate at the surface experiencing bending and axial tensile strain. The strain continues to increase and progress along the cross section, and then tends to become more uniform along the section. Photostress provided excellent snapshots of the progressive weld acreage response, but irrelevant to the detailed nonhomogeneous modeling demanded by this investigation.

IV. SUMMARY AND CONCLUSIONS

In-plane loading is the preferred strength application of butt welds, but these same loads can induce bending when allowed to advance into abrupt geometric changes. Weld fillers, having the lowest elastic limit and limited width (gauge length), will yield first and progressively distort most in bending. This principle was especially appreciated in this investigation. The multipass weld structural analyses were based on experimental strain data from a double U-groove aluminum weldment, from which two welding process sources were identified for improving the weld strength under uniaxial loading. Both were related to peaking.

The extreme thermal expansion and contraction of the second fusion weld heat produces severe peaking with the obtuse angle on the heat source side of the panels. The peaking eccentricity induces a bending moment under uniaxial loading which initiates yield that progresses through the cross section creating elastic and inelastic zones. These zones having different stiffness shift the bending neutral axis from the midplane and increase the bending moment. Both eccentricities reduce the weld strength over a uniformly distributed loading. Current peaking reduction is achieved through a normal weld schedule in which subsequent filler weld passes are serially applied first in the groove opposite the fusion pass, and then the filler passes are completed in the second groove.

A depeaking index model was developed to determine the relative depeaking achieved through varying the filler pass thickness, the number of passes, and the groove side sequence scheduling. It turned out that the groove side receiving the thicker and most filler passes earliest produced the greater relative depeaking angle. Off-centering the tabs between the U-grooves produce even greater depeaking.

The other weld process phenomenon was that the filler pass inelastic properties varied across the weld thickness with the weld pass yield stress decreasing with increasing sequence number. The last weld pass was noted to have the lowest yield property, the prior pass had the next lowest yield property, etc. This phenomenon coincided with the decreasing peaking index model.

Since filler depeaking and strain hardening decreases with increasing passes, later filler passes experience less strain hardening which acquire less heat treatment to produce lower yield stress.

Consequently, if the weaker last pass filler (on obtuse angle of the specimen) is combined with the tension component of the induced moment, the last pass filler will prematurely rupture under uniaxial loading. A significant improvement would depeak the weld sufficiently to reverse the obtuse angle to the first pass side in order to induce the tension component of the moment on the earlier passes having higher yield and ultimate strengths.

Another weld design consideration is that increasing the tab thickness between the double U-grooves increases the fusion weld heat rate input, which increases the thermal expansion and contraction gradient, producing greater peaking. Also increasing the tab thickness of the milled plates proportionally increases the net weld strength over the weaker filler casting-like material. It should be a simple trade among other manufacturing parameters that invites exploration.

While an earlier study established the parent-filler interface to be the weakest region in a butt-weld, this experimental investigation developed a model to improve the net weld strength through welding process options. Characterizing the tab size with peaking rate should further extend the fundamental mechanics of thick welds.

REFERENCES

1. Verderaime, V.: "Plate and Butt-Weld Stresses Beyond Elastic limits." NASA TP-3075, January 1991.

2. Kerkof, S.: "AFT Skirt Weld Analysis Methods." United Technology, USBI, presentation to MSFC, April 16, 1991.

3. Gambrell, S.: "Use of Photostress and Strain Gauges to Analyze Behavior of Weldments." NASA/MSFC Contract No. NAG 8-293, Sub 93-101, University of Alabama, Tuscaloosa, AL, 1993.

4. Vaughan, R.: "An Inelastic Analysis of a Weld Aluminum Joint." NASA TP-3508, September 1994.

5. Sechler, E.E.: "Stress Rise Due to Offset Welds in Tension." Space Technology Laboratories, Inc., Report No. EM9-18, August 28, 1959.

6. Timoshenko, S., and Goodier, J.: "Theory of Elasticity." McGraw-Hill Book Co., 1951.

7. Dong, P., and Lippold, J.: "FEM of Residual Stresses in Alloy 2195 Weldments for SLWT Applications." EWI Final Report J8828-1, August 1994.

8. Anonymous: "Structural Factor of Safety and Test Verification." NASA white paper, October 9, 1992.

9. Phillips, A.: "Introduction to Plasticity." The Ronald Press Company, 1956.

10. Dieter, G.: "Mechanical Metallurgy." Third edition, McGraw-Hill, Inc., NY, 1986.

11. Anonymous: MIL-Handbook C5 "Metallic Materials and Elements for Aerospace Vehicle Structures." September 1976.

12. Gambrell, S.: "Use of Photostress and Strain Gauges to Analyze Behavior of Weldments." Summary of NASA/ASEE Fellowship Program, May 1991.

APPENDIX A

EXPERIMENTAL DATA

Data listed in table A1 are based on "first loading" uniaxial tests from a common specimen as reported by Dr. S. Gambrell in reference (3). Gauge numbers 1, 5, 6, and 10 are surface mounted and the other gauges are mounted along the specimen cross section as shown in figure 5.

Table A1. Axial loads versus strain experimental data.

Gauge Number	5 kips	10	15	20	25	30	35	40
Filler								
1	0.0008	0.0015	0.0026	0.0040	0.0063	0.0104		
2	0.0005	0.0010	0.0016	0.0024	0.0034	0.0056	0.0118	
3	0.0004	0.0009	0.0014	0.0020	0.0028	0.0040	0.0070	
4	0.0004	0.0008	0.0013	0.0018	0.0026	0.0037	0.0070	0.0140
5	0.0004	0.0006	0.0010	0.0012	0.0016	0.0029	0.0032	0.0080
HAZ								
6	0.0006	0.0012	0.0018	0.0024	0.0032	0.0054	0.0098	
7	0.0007	0.0011	0.0017	0.0024	0.0031	0.0043	0.0065	0.0139
8	0.0004	0.0008	0.0014	0.0020	0.0028	0.0040	0.0060	0.0106
9	0.0006	0.0010	0.0014	0.0019	0.0025	0.0032	0.0043	0.0066
10	0.0005	0.0008	0.0012	0.0016	0.0020	0.0026	0.0038	0.0074

APPENDIX B

MATERIALS MODELING

Because structural behavior of welds is about material properties, a review of basic aluminum mechanical properties is essential to the collective evaluation, approximation, and modeling strain responses of multipass welds. The base and filler aluminum materials of the weld specimen are of a polycrystalline nature having face-centered-cubic lattice microstructure which distinguishes their thermal, stiffness, displacement, and strength behaviors from other microstructures.

Uniaxial Stress-Strain Relationships

The single most common observation of polycrystalline mechanical behavior is the uniaxially applied stress and the measured strain response. Uniaxial tension tests are the simplest type for obtaining the most commonly used properties of homogeneous structural materials. Figure B1 typifies the elastic and inelastic stress-strain relationship of a polycrystalline material achieved from such a test. The segment $O-\sigma_o$ is the linear elastic range of the material which is governed by the resilience between atoms within a crystal lattice and defined by two constants. Applying the analogy of spring energy interaction between atoms to the elastic space lattice concept, springs between corner atoms define Hooke's spring constant $E = \sigma / \varepsilon$, and all diagonal springs feature the volume related constant defined by Poisson's ratio, $v_e = -\varepsilon_y/\varepsilon_x$. When the applied stress is relieved, the elastic deformation recovers to its original position, "0".
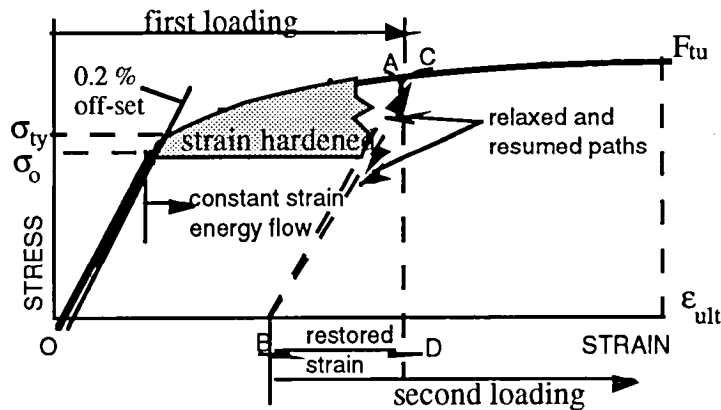
Figure B1. Uniaxial tensile properties of polycrystalline materials.

The limit of these elastic properties is reached when atoms displace along cleavage planes and plastic flow occurs at constant strain energy within atomic bonds. Plastic flow is the permanent deformation caused by the displacement of atoms to new crystal lattice sites. The ratio of elastic stress and plastic flow defines the inelastic slope, and their change rate characterizes the nonlinear property of the material beyond the stress elastic limit, σ_o, up to the ultimate stress, F_{tu}. Aluminum's face-centered-cubic lattice provides many slip planes to make it more ductile than other cubic microstructures.

When the uniaxial specimen is "first loaded" beyond the elastic limit to point "A" and relaxed, the strain decreases elastically to point "B". The material will have restored the elastic

strain *B-D*, but will have permanently deformed and spent a plastic strain of *O-B*. Upon "second loading," the unit load traces a hysteresis loop as it approaches point "*C*" near point "*A*" from which it was unloaded and then resumes the stress-strain relationship as if it had not relaxed. This is a very important hardening feature which was assumed above to occur in the multipass welding process.

Plastic deformation starts in different locations, numbers, and intensities, and it is difficult to detect and determine where and how much deformation progressed until large enough parts have been affected. This phenomenon explains why different gauge lengths in uniaxial tensile tests provide different elastic limits. Hence, an arbitrarily selected standard for defining the yield point is the intersection of a line parallel to and offset by 0.2 percent from the elastic stress-strain slope.

Dislocation is the separation of the slipped and unslipped regions of a crystal, and strain hardening is due to dislocation interactions and pileups. Cold-working increases strain hardening, which increases the slope, and is more effective on cubic lattice materials. Cold-working also produces anisotropy properties as in milled stock. Aluminum strength of the specimen is further increased through age hardening, which occurs when critical size particles are formed and act as slip-prevention keys in crystallographic planes of weakness. Heating accelerates the particle formation, but excessive heat produces larger and fewer particles which decrease the strength. These elastic-inelastic property variations are reflected in uniaxial test data.

Elastic-Inelastic Modeling

Modeling inelastic behavior could be very difficult unless idealized into the simplest mathematical expressions within the physical phenomena of the material and its application. While there are many approaches and techniques[9] for modeling inelastic properties to classical strength of materials elements, the approach used in this study was to model the total range of elastic-inelastic uniaxial stress-strain relationship of figure B1 with a two parameter power expression,[10]

$$\sigma = K \varepsilon^n .$$

(B1)

The exponent "*n*" is the strain-hardening exponent and "*K*" is the strength coefficient of an inelastic material. An exponent $n = 0$ defines a perfectly plastic solid. An elastic material is defined by $n = 1.0$ and the proportionality constant E of Hooke's law is substituted for K. Auspiciously, inelastic models using this expression may be directly and conveniently converted into elastic models.

To illustrate basic inelastic properties in related aluminum materials, figure B2 delineates the stress-strain relationship of three temper designation of 2219 plates[11] and a 2319 weld filler.[12] All four plots are noted to have a common elastic modules of $E = 10,500$ ksi, and all four plots demonstrate similar strain hardening curves, which are tied by their common face-centered-cubic lattice substructure and copper alloy. Their strength dispersions are fixed by their temper processes which establish their unique elastic stress limit and strain hardening slope. Modeling the temper dispersions of typical materials in figure B2 is required to correlate weld specimen test data with material condition.
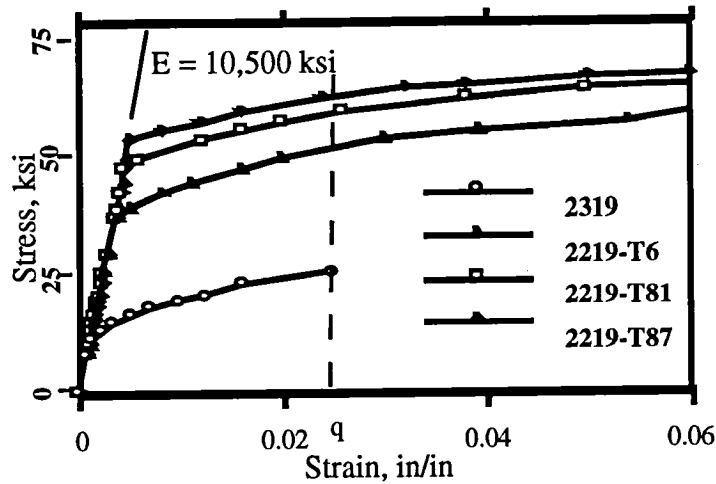
Figure B2. Relationships of 2219 aluminum tempers.

Because of their common lattice structure and alloys, modeling elastic-inelastic stress and strain properties of different tempers was simplified by characterizing their relative slopes. The elastic modulus $E = 10,500$ ksi is thus common to all tempers. Curve-fitting equation (B1) to a specific inelastic stress-strain temper, the stress and associated strain at the extreme ends of the inelastic curve provide the necessary two equations and two inelastic parameters. The yield point must necessarily define one end of the curve for continuity from elastic to inelastic curve, and the second set may be at any point of extreme interest "q" including ultimate stress and strain. A "q" related to a common inelastic strain of $\varepsilon_q = 0.06$ should accommodate all tempers required in this study. Applying yield and ultimate stress and associated strain properties to equation (B1), the strain hardening exponent is expressed by

$$n = \frac{\log (F_q/F_{ty})}{\log (E \, \varepsilon_q/ F_{ty})} \; ,$$ (B2)

and the strength coefficient is

$$K = E^n F_{ty}^{(1-n)} \; .$$ (B3)

The inelastic stress-strain slopes of any temper "k" are seen in figure B2 to vary linearly with yield stresses. Given the yield stress of any temper, the strain hardening exponent (slope) may be shown to be approximated by the linear expression,

$$n_k = 0.34 - 0.0045 \, F_{ty,k} \; ,$$ (B4)

and the strength coefficient is similar to equation (B3)

$$K_k = E^n F_{ty,k}^{(1-n_k)} \; .$$ (B5)

Equation (B4) is an interesting approximation in that calculating the yield stress from an identified yield strain from table A1, the inelastic property of a weld pass or panel may be determined.

Applying these models to the tempers in figure B2, the elastic and inelastic properties are summarized in table B1.

Table B1. Al 2219 temper properties.

Materials	F_q	F_{ty}	ε_q	ε_{ty}	n	K	n_k	Percent Error
2219-T87	68	53	0.06	0.0050	0.100	90.2	0.101	1.0
2219-T81	66	48	0.06	0.0045	0.123	93.5	0.124	0.1
2219-T6	58	38	0.06	0.0033	0.174	94.8	0.182	4.6
2319 Filler	26	10	0.06	0.0009	0.296	78.5	0.295	0.0

Perfectly plastic materials are assumed to be incompressible. A zero volume change provides the ideal plastic Poisson's ratio of $v_e = 0.5$. An inelastic Poison's ratio between yield and ultimate stresses may be related to the secant modules defined by the stress-strain model of equation (B1) and approximated by:

$$v = v_p - \left(v_p - v_e\right)\frac{\sigma}{E}\left[\frac{K}{\sigma}\right]^n ,$$
(B6)

and where $n = 1$ and $K = E$, equation (B6) appropriately degenerates into the elastic Poisson's ratio, $v_e \approx 0.3$.

Another influential aluminum property discussed in the welding process was the thermal coefficient of expansion approximated by

$$\alpha = 9.1 \times 10^{-6} \, T^{0.06} \, \text{in/in/°F} \quad \text{for} \quad T \le 500 \, \text{°F} ,$$
(B7)

which is over 30 percent greater than steel, and more sensitive on multipass thermal residual bending.

APPENDIX C

STRUCTURAL MODELING

The weld test specimen data was noted to be subjected to a predominant applied axial load combined with induced bending, figure 8, which varied with increasing test loading through the elastic and inelastic range of the materials. Given back-to-back surface measured strain data and assuming a rectangular cross section of thickness "H," and width "w," it was required to determine the axial loads "N" and the bending moment "M." Material properties are modeled in appendix B. Because surface strain data are shown to increase from elastic through inelastic range, the analyses were modeled with inelastic parameters and converted to elastic models through substitutions of $n = 1$ and $K = E$ as required.

Modeling first the pure normal and pure bending loads, the normal stress acting on the cross section is

$$\sigma_N = \frac{N}{wH} , \tag{C1}$$

and using equation (B1), the corresponding strain is

$$\varepsilon_N = \left[\frac{N}{KwH} \right]^{\frac{1}{n}} . \tag{C2}$$

Cross sectional planes remain plane in elastic and inelastic bending, and the midplane ($H/2$) of the cross section and the bending neutral axis are coincident from which the bending strain is linearly proportional along the thickness. The bending stress at the extreme fibers is shown[1] to be

$$\sigma_M = \pm \frac{2\,(n+2)\,M}{w\,H^2} . \tag{C3}$$

Substituting equation (C3) into equation (B1) gives the bending strains at the extreme fibers,

$$\varepsilon_M = \pm \left[\frac{2\,(n+2)\,M}{K\,w\,H^2} \right]^{\frac{1}{n}} , \tag{C4}$$

and the maximum bending transverse displacement on a cantilevered element is

$$y = -\frac{\ell^2}{2} \left[\frac{(n+2)\,M}{2Kw\,(H/2)^{(n+2)}} \right]^{\frac{1}{n}} . \tag{C5}$$

Because inelastic axial normal-bending stresses are not linearly related to strains, they cannot be directly superimposed nor is the bending neutral axis expected to coincide with the section mid-plane. Since plane strains remain plane after pure bending, they are linearly proportional to the strain at the extreme fiber, "ε_M", and may be algebraically added to the uniformly linear normal strain "ε_N," as shown in figure C1. These combined strains are measured at the surfaces as ε_A and ε_B.

26

Figure C1(b) illustrates the nonlinear bending stress distribution derived from the strain distribution using equation (1).

(a) Strain distributions   (b) Stress distributions
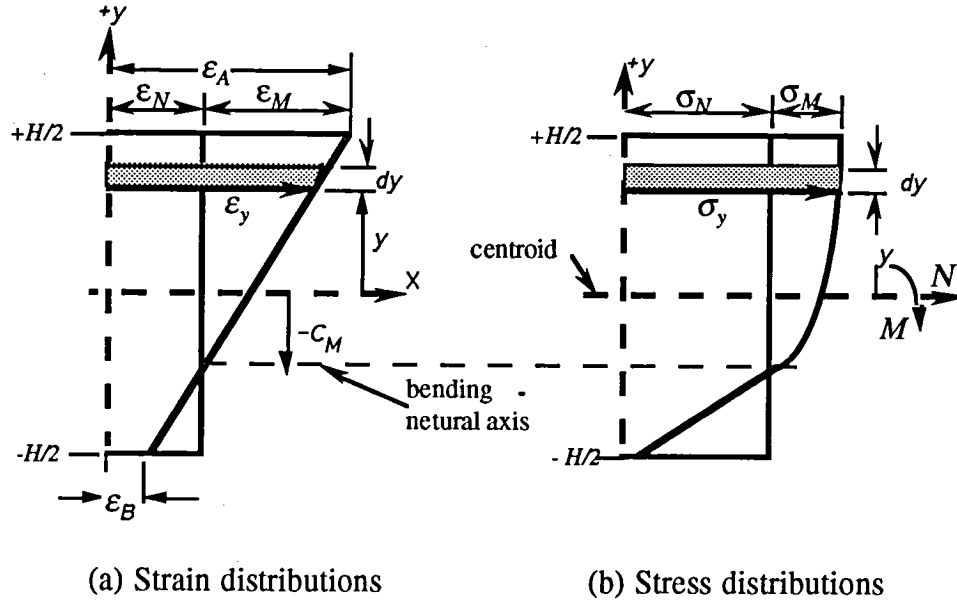
Figure C1. Bending and normal strain and stress profiles along the thickness.

Since the elastic as well as the inelastic linear strains are mutually linear, figure C1(a) is an appropriate diagram to derive linear variables and relationships required for the analysis. Using the two back-to-back surfaces measured strains, and always assuming $\varepsilon_A > \varepsilon_B$, the objective is to identify the strain distribution profile, define the elastic and inelastic zones, their boundaries limits, and their normal and bending loads in the profile.

The net strain from any midplane y-distance along the element thickness in figure C1(a) is defined by the proportionality

$$\frac{\varepsilon_y - \varepsilon_B}{\varepsilon_2 - \varepsilon_1} = \frac{\frac{H}{2} + y}{H} \ ,$$

or

$$\varepsilon_y = \gamma \, (0.5 \, H + y) + \varepsilon_B \ , \tag{C6}$$

and

$$y = \frac{1}{\gamma} \, (\varepsilon_y - \varepsilon_B) - 0.5 \, H \ . \tag{C7}$$

The bending strain slope is

$$\gamma = \frac{\varepsilon_A - \varepsilon_B}{H} \ . \tag{C8}$$

The incremental normal load along the cross section thickness is the product of the induced stress and unit area,

$$dN = w \sigma_y \, dy = w K \left(\varepsilon_y \right)^n dy \ .$$

Substituting equation (C6) for the strain and integrating, zone normal loads are calculated from

$$N_k = \frac{wK\gamma^n}{n+1} \left[\frac{H}{2} + \frac{\varepsilon_B}{\gamma} + y \right]^{n+1} \Big]_{C_b}^{C_a} , \tag{C9}$$

where $C_a > y > C_b$ are the integration limits of a zone. A zone is bound along the y-axis by the surface measured strains, ε_A and ε_B, or by the material limit changes noted by the yield tensile strain, ε_{ty}, a distance C_{ty} from the midplane. Substituting the appropriate pair of boundary strains into equation (C7),

$$C_{a,b} = \frac{1}{\gamma} \left(\varepsilon_{a,b} - \varepsilon_B \right) - \frac{H}{2} , \tag{C10}$$

provides the upper and lower integration limits of a zone. The normal load across the thickness is the algebraic sum of all the zone normal loads

$$N = \sum N_i . \tag{C11}$$

Bending strain along the thickness is given by $\varepsilon_{My} = \varepsilon_y - \varepsilon_N$, and the neutral bending axis is located where the bending strain is zero ($\varepsilon_{My} = 0$). Substituting $\varepsilon_y = \varepsilon_N$ into equation (C7), the neutral bending axis is

$$C_M = \frac{1}{\gamma} \left(\varepsilon_N - \varepsilon_B \right) - 0.5 H , \tag{C12}$$

where the normal strain, ε_N, across the thickness is determined by substituting equation (C11) into equation (C2). The incremental normal load acting about the bending axis of equations (C12) gives the incremental moment

$$dM = w\sigma_y(y - C_M)\, dy = wK \left(\varepsilon_y \right)^n (y - C_M)\, dy ,$$

and substituting equations (C6) and (C12) and integrating, the moment of a zone about the neutral axis is calculated from

$$M_i = wK\gamma \left[\frac{H}{2} + \frac{\varepsilon_B}{\gamma} + y \right]^{n+1} \left\{ \frac{\frac{H}{2} + \frac{\varepsilon_B}{\gamma} + y}{n+2} - \frac{\frac{H}{2} + \frac{\varepsilon_B}{\gamma} + C_M}{n+1} \right\} \Bigg]_{C_b}^{C_a} . \tag{C13}$$

The total moment acting over the thickness is

$$M = \sum M_i . \tag{C14}$$

A unit width, $w = 1$, is assumed for plates and shells from which normal loads and bending moments are defined as kips-per-inch and kip-inch-per-inch units, respectively. Using the strain distribution expression of equation (C6), the stress distribution along each zone is given by

$$\sigma_y = K \left[ABS \left(\varepsilon_y \right) \right]^n SGN \left(\varepsilon_y \right) . \tag{C15}$$

Expressions shown in absolute form allow raising strains to odd powers. $SGN(\ )$ is the signum function, which reestablishes the sign of the expression.

These models and related integration limits are the means for analyzing induced loads and stress and strain distributions for any of the probable elastic-inelastic strain profiles shown in figure C2.

$$(I)\ \varepsilon_B<\varepsilon_A<\varepsilon_{ty} \quad (II)\varepsilon_B<\varepsilon_{ty}<\varepsilon_A \quad (III)\ \varepsilon_{ty}<\varepsilon_B<\varepsilon_A$$
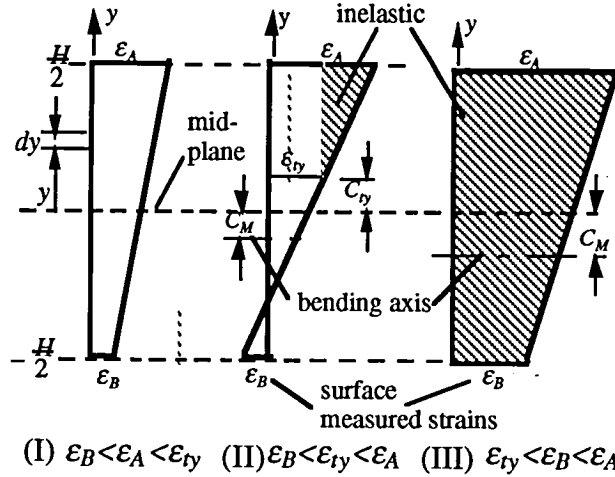
Figure C2. Strain profiles over element cross section defined by measured surface strains.

Given the values of the two measured strains, ε_A and ε_B, the related profile in figure C2 is directly selected and the zones and integration limits are defined as shown. The analysis then proceeds as follows:

- Using strains at zone boundaries noted in figure C2 profile, integration limits $C_{a,b}$ are calculated from equation (C10) and substituted into equation (C9) to solve for the normal load $N_{I,k}$ of each zone in the profile.

- Normal loads in the profile are summed by equation (C11) and substituted into equation (C2) to obtain the profile normal strain, ε_N.

- The bending neutral axis C_M is located by using the total normal strain ε_N in equation (C12).

- The bending moment $M_{I,k}$ in each zone about the neutral bending axis is calculated from equation (C13).and summed for the profile as in equation (C14).

- Distributions of strain ε_y and stress $_y$ over the thickness are plotted from equations (C2) and (C15), respectively.

Profile (II), having double zones, was solved and programmed as outlined. Other profiles, having a single zone, were adapted by resetting integration limits to their zone $+H/2$ and $-H/2$ boundary values noted in figure C2.

29

```
0 'NORMAL/BENDING LOADS FROM STRAIN test
'NMweld, Microsoft Quick Basic

' MATERIAL PROPERTIES
INPUT "ELASTIC MODULUS E=";ELM
INPUT "YIELD STRESS Fty=";FTY
INPUT "MAX STRESS Ftu=";FTU
INPUT "STRAIN @ MAX STRESS Etu=";ETU

ETY=FTY/ELM
PRINT "TENSION YIELD STRAIN";ETY
SHE=LOG(FTU/FTY)/LOG(ETU/ETY)
PRINT "STRAIN HARDENING EXPO. n=";SHE
K=FTY/(ETY^SHE)
PRINT "STRENGTH COEF K=";K
K0=K
SHE0=SHE
ETY0=ETY

'TEST DATA
INPUT "RECT BAR THICKNESS H=";H
INPUT "BAR WIDTH w=";W

10 INPUT "SURFACE MAX STRAIN EA=";E2
INPUT "SURFACE MIN STRAIN EB=";E1
.IF E2<E1 THEN
PRINT "MAX STRAIN < MIN STRAIN"
GOTO 10
END IF
IF E2=E1 THEN E1=.975
 SLOP=(E2-E1)/H

PRO=2
'USING PROFILE (II) (E1<ETY<E2)
IF ETY<E1 AND E1<E2 THEN
ETY=E1:PRO=3
ELSEIF E2<ETY THEN
K=ELM :SHE=1:ETY=E2:PRO=1
END IF

NII1=W*K*(E2^(SHE+1)-ETY^(SHE+1))
NII1=NII1/(SLOP*(SHE+1))
NII2=W*ELM*((ETY^2)-(E1^2))/(2*SLOP)
NIIT=NII1+NII2
PRINT "TOTAL AXIAL LOAD N=";NIIT
SNII=NIIT/W/H
PRINT "AXIAL LOAD STRESS SN=";SNII

IF SNII<FTY THEN
ENII=SNII/ELM
ELSE
ENII=(SNII/K)^(1/SHE)
END IF
PRINT "AXIAL LOAD STRAIN EN=";ENII
EMMII=E2-ENII
PRINT "MAX BENDING STRAIN EM=";EMMII

CMII= (ENII-E1)/SLOP-H/2
PRINT "BENDING NEUTRAL AXIS CM=";CMII

MII1=-((E2^(SHE+1))-(ETY^(SHE+1)))/(SHE+1)
MII1=MII1*((E1+E2)/2+CMII*SLOP)
MII1=MII1+((E2^(SHE+2))-(ETY^(SHE+2)))/(SHE+2)
MII1=MII1*W*K/(SLOP^2)
MII2=-((ETY^2)-(E1^2))*((E1+E2)/2+CMII*SLOP)/2

MII2=MII2+((ETY^3)-(E1^3))/3
MII2=MII2*W*ELM/(SLOP^2)
MIIT=MII1+MII2
PRINT "BENDING MOMENT M=";MIIT

RII=MIIT/NIIT
PRINT"MOMENT/AXIAL LOAD RATIO R=";RII

PrintScreen 0,0,0

'LIMITS
CTY=(ETY-E1)/SLOP-H/2
ETYA=FTY/ELM

' STRESS & STRAIN DISTRIBUTIONS
OPEN "CLIP:" FOR OUTPUT AS No. 2

PRINT "PROFILE=";PRO

IF PRO=1 OR PRO=2 THEN
YS=-.5*H: YF=CTY: MY=9
M=MY-1
DY=(YF-YS)/M
EY2=0: SY2=O
y=YS
FOR I=1 TO M
EY2=(.5*H+y)*SLOP+E1
SY2=ELM*EY2
WRITE No. 2,y,EY2,ENII,ETYA,SY2,SNII,FTY
PRINT y,EY2,ENII,ETYA,SY2,SNII,FTY
y=YS+(I+1)*DY
NEXT I
END IF

IF PRO=2 OR PRO=3 THEN
YS=CTY: YF=.5*H: MY=11
M=MY-1
DY=(YF-YS)/M
EP1=0: SP1=0
y=YS
FOR I=1 TO M
EP1=(.5*H+y)*SLOP+E1
SP1=K*((ABS(EP1)^SHE))*SGN(EP1)
WRITE No. 2,y,EP1,ENII,ETYA,SP1,SNII,FTY
PRINT y,EP1,ENII,ETYA,SP1,SNII,FTY
y=YS+(I+1)*DY
NEXT I
END IF

CLOSE No. 2
REM STOP
CLS
ETY=ETY0
K=K0
SHE=SHE0
GOTO 10

SUB PrintScreen(scale%,x%,y%) STATIC
 ' CALCULATE ARRAY SIZE NEEDED TO GET ENTIRE
SCREEN
max&=((4+(SYSTEM(6)+1)*2*INT(SYSTEM(5)+16)/16))/4+1
 IF max&>32767 OR max&*4+60>FRE(0) THEN BEEP:EXIT
SUB
 DIM pt%(1),screen&(max&) 'pt%() will contain 0,0
 LocalToGlobal pt%(0) 'Find window position on screen
```

30

```
 GET (-pt%(1), -pt%(0)) - (SYSTEM(5)-pt%(1),SYSTEM(6)-
pt%(0)),screen&
 ' "prompt" allows user to select an orientation so the dump will
 ' fit on a page.
 OPEN "LPT1:prompt" FOR OUTPUT AS No. 10
 WINDOW OUTPUT No. 10
 IF scale% THEN PUT(0,0)-(x%,y%), screen& ELSE
PUT(0,0),screen&
 CLOSE No. 10
 ERASE pt%,screen& 'release memory
END SUB
0 !0!
```

REPORT DOCUMENTATION PAGE

Form Approved OMB No. 0704-0188

Public reporting burden for this collecton of information is estimated to average 1 hour per response, including the time for reviewing instructions, searching existing data sources, gathering and maintaining the data needed, and completing and reviewing the collection of information. Send comments regarding this burden estimate or any other aspect of this collection of information, including suggestions for reducing this burden, to Washington Headquarters Services, Directorate for Information Operations and Reports, 1215 Jefferson Davis Highway, Suite 1204, Arlington, Va 22202-4302, and to the Office of Management and Budget, Paperwork Reduction Project (0704-0188), Washington, DC 20503.

1. AGENCY USE ONLY (Leave Blank)	2. REPORT DATE August 1995	3. REPORT TYPE AND DATES COVERED Technical Paper

4. TITLE AND SUBTITLE

Aluminum U-Groove Weld Enhancement Based on Experimental Stress Analyses

5. FUNDING NUMBERS

6. AUTHOR(S)

V. Verderaime and R. Vaughan

7. PERFORMING ORGANIZATION NAME(S) AND ADDRESS(ES)

George C. Marshall Space Flight Center
Marshall Space Flight Center, Alabama 35812

8. PERFORMING ORGANIZATON REPORT NUMBERS

M-789

9. SPONSORING/MONITORING AGENCY NAME(S) AND ADDRESS(ES)

National Aeronautics and Space Administration
Washington, DC 20546-0001

10. SPONSORING/MONITORING AGENCY REPORT NUMBER

NASA TP-3581

11. SUPPLEMENTARY NOTES

Prepared by Structures and Dynamics Laboratory, Science and Engineering Directorate.

12a. DISTRIBUTION/AVAILABILITY STATEMENT

Unclassified-Unlimited
Subject Category 15

12b. DISTRIBUTION CODE

13. ABSTRACT *(Maximum 200 words)*

Though butt-welds are among the most preferred joining methods in aerostructures because of their sealing and assembly integrity and general elastic performance, their inelastic mechanics are generally the least understood. This study investigated experimental strain distributions across a thick aluminum U-grooved weld and identified two weld process considerations for improving the multipass weld strength. The extreme thermal expansion and contraction gradient of the fusion heat input across the tab thickness between the grooves produce severe peaking, which induces bending moment under uniaxial loading. The filler strain hardening decreased with increasing filler pass sequence. These combined effects reduce the weld strength, and a depeaking index model was developed to select filler pass thicknesses, pass numbers, and sequences to improve the welding process results over the current normal weld schedule.

14. SUBJECT TERMS
weld improvement, weld peaking stress, weld peaking reduction, weld pass properties, U-groove weld analysis, thick weld stresses

15. NUMBER OF PAGES 40

16. PRICE CODE A03

17. SECURITY CLASSIFICATION Unclassified	18. SECURITY CLASSIFICATION OF THIS PAGE Unclassified	19. SECURITY CLASSIFICATION OF ABSTRACT Unclassified	20. LIMITATION OF ABSTRACT Unlimited

NSN 7540 - 01 - 280 - 5500

Standard Form 298 (Rev 2-89)

National Aeronautics and
Space Administration
Code JTT
Washington, DC
20546–0001

Official Business
Penalty for Private Use, $300

Postmaster: If Undeliverable (Section 158 Postal Manual), Do Not Return